

Multiwavelength radio observations of a Brightest Cluster Galaxy at $z=1.71$: Detection of a modest Active Galactic Nucleus and evidence for extended star formation

Ariane Trudeau^{1,2,3*}, Tracy Webb², Julie Hlavacek-Larrondo³, Allison Noble⁴, Marie-Lou Gendron-Marsolais⁵, Christopher Lidman⁶, Mar Mezcua^{7,8}, Adam Muzzin⁹, Gillian Wilson¹⁰, H. K. C. Yee¹¹

¹Department of Physics & Astronomy, University of Victoria, 3800 Finnerty Road, Victoria, British Columbia, V8W 2Y2, Canada

²Department of Physics, McGill University, 3600 rue University, Montréal, Québec, H3P 1T3, Canada

³Département de Physique, Université de Montréal, Succ. Centre-Ville, Montréal, Québec, H3C 3J7, Canada

⁴MIT Kavli Institute for Astrophysics & Space Research, 77 Massachusetts Avenue, Cambridge, MA 02139, USA

⁵European Southern Observatory, Alonso de Córdova 3107, Vitacura, Casilla 19001, Santiago, Chile

⁶The Research School of Astronomy and Astrophysics, Australian National University, ACT 2601, Australia

⁷Institute of Space Sciences (ICE, CSIC), Campus UAB, Carrer de Magrans, E-08193 Barcelona, Spain

⁸Institut d'Estudis Espacials de Catalunya (IEEC), Carrer Gran Capità, E-08034 Barcelona, Spain

⁹Department of Physics & Astronomy, York University, 4700 Keele St., Toronto, Ontario, Canada, M3J 1P3

¹⁰Department of Physics & Astronomy, University of California Riverside, 900 University Avenue, Riverside, CA 92521, USA

¹¹Department of Astronomy & Astrophysics, University of Toronto, 50 St. George Street, Toronto, ON, M5S 3H4, Canada

Accepted 2019 May 14. Received 2019 May 3; in original form 2019 February 16

ABSTRACT

We present deep, multiwavelength radio observations of SpARCS104922.6+564032.5, a $z = 1.71$ galaxy cluster with a starbursting core. Observations were made with the *Karl G. Jansky Very Large Array* (JVLA) in 3 bands: 1–2 GHz, 4–8 GHz and 8–12 GHz. We detect a radio source coincident with the Brightest Cluster Galaxy (BCG) that has a spectral index of $\alpha=0.44\pm 0.29$ and is indicative of emission from an Active Galactic Nucleus. The radio luminosity is consistent with the average luminosity of the lower redshift BCG sample, but the flux densities are 6σ below the predicted values of the star-forming Spectral Energy Distribution based on far infrared data. Our new fit fails to simultaneously describe the far infrared and radio fluxes. This, coupled with the fact that no other bright source is detected in the vicinity of the BCG implies that the star formation region, traced by the infrared emission, is extended or clumpy and not located directly within the BCG. Thus, we suggest that the star-forming core might not be driven by a single major wet merger, but rather by several smaller galaxies stripped of their gas or by a displaced cooling flow, although more data are needed to confirm any of those scenarios.

Key words: galaxies: active – galaxies: clusters: individual (SpARCS104922.6+564032.5) – galaxies: evolution – galaxies: interactions – galaxies: starburst – radio continuum: galaxies

1 INTRODUCTION

The most massive galaxies in the Universe lie at the centre of galaxy clusters. In comparison with field galaxies, these objects, called Brightest Cluster Galaxies (BCGs), exhibit unique properties such as distinct luminosity and surface brightness profiles (e.g. Oemler 1976; Tremaine & Richstone 1977; Dressler 1978). We still do not understand how exactly

BCGs acquired these distinct properties. Nevertheless, we suspect that environmental effects and their distinct formation histories might explain why they developed specific brightness profiles and luminosities.

On larger scales, the clusters in which BCGs reside can generally be divided into two categories: cool core clusters, which exhibit very peaked surface brightness distributions at X-ray wavelengths, and non cool core clusters, with similar overall X-ray luminosities but with smoother, less peaked X-ray surface brightness distributions. Some authors (e.g. Hudson et al. 2010; Santos et al. 2010) define an

* Contact e-mail: arianetrudeau@uvic.ca

intermediate category called moderate or weak cool core clusters. Since cool core clusters have short radiative cooling time-scales on the order of 10^8 years in their centres (e.g. Voigt & Fabian 2004; McNamara & Nulsen 2007, 2012; Hlavacek-Larrondo et al. 2012), starbursts are expected to be common at the centre of such clusters. Indeed, the central cool gas in these clusters should condense onto the BCG, forming stars at rates of hundreds of solar masses per year (e.g. Fabian 1994). However, most BCGs are relatively quiescent and those that do show evidence of star formation generally tend to have star formation rates one order of magnitude smaller, on the order of $1 - 150 M_{\odot} \text{ yr}^{-1}$ (e.g. Donahue et al. 2007; Bildfell et al. 2008; O’Dea et al. 2008, 2010; Rawle et al. 2012).

This mismatch between expected and observed star-forming rates, known as the cooling flow problem, is thought to be caused by Active Galactic Nuclei (AGN) feedback processes from the BCG. AGNs can release copious amounts of energy into the intracluster medium (ICM) through many ways, including: jetted outflows that inflate cavities, weak shocks, sound waves or turbulence in the ICM (e.g. McNamara & Nulsen 2007, 2012; Markevitch & Vikhlinin 2007; Zhuravleva et al. 2014; Fabian et al. 2017). Alone, the energy released by jetted outflows appears to be on the same order as the energy needed to offset cooling (e.g. Rafferty et al. 2006; McNamara & Nulsen 2007; Hlavacek-Larrondo et al. 2012), therefore suggesting that AGN feedback is a good candidate for solving the cooling flow problem.

According to semi-analytic models (e.g. De Lucia & Blaizot 2007) and to several hydrodynamical simulations (e.g. Ragone-Figueroa et al. 2018) it has been proposed that star formation occurs very early in BCG history (mostly before $z \sim 3$) and is quickly suppressed by AGN feedback (e.g. Croton et al. 2006). Later, BCGs are thought to be built-up by dry mergers, without significant star formation. This scenario is supported by several mass growth measurements of BCGs, mostly below $z \sim 1$ (e.g. Stott et al. 2008, 2011; Lidman et al. 2012; Bellstedt et al. 2016), although authors disagree on the mass growth rate. For example, Stott et al. (2011) measured a growth rate of 30% between a redshift of $z = 1$ and $z = 0.25$, while Lidman et al. (2012) found that BCG sizes increase by a factor of 1.8 ± 0.3 between $z \sim 0.9$ and $z \sim 0.2$.

At $z > 1$, however, there are growing divergences between this scenario and observations: Webb et al. (2015b) and McDonald et al. (2016) both find evidence of significant in-situ star formation in BCGs at $z \gtrsim 1$. We don’t know what the star formation triggering mechanism is, but gas-rich galaxy interactions are a possibility. For example, according to McDonald et al. (2016), star-forming BCGs seem to preferentially lie in dynamically unrelaxed, non-cool core clusters.

SpARCS104922.6+564032.5 (hereafter referred as SpARCS1049), located at $z = 1.7089$ (Webb et al. 2015a), provides additional evidence for this scenario. It is one of the most distant spectroscopically confirmed clusters known to date and was discovered by the *Spitzer Adaptation of the Red-sequence Cluster Survey* (SpARCS) collaboration (e.g. Muzzin et al. 2009; Wilson et al. 2009; Demarco et al. 2010).

The complex morphology of the BCG in SpARCS1049, revealed by the *Hubble Space Telescope* (see Figure 1) suggests that this BCG has been caught in the process of a major merger (Webb et al. 2015a). The single, large backward J-like tidal tail and the chain of clumps are reminiscent of ‘shrimp-like’ interacting galaxies, as defined by

Elmegreen et al. (2007). The clump chain seems to originate from within the stellar halo of the BCG and has a linear extent of ~ 60 kpc.

The cluster core, including the BCG, a pair of interacting cluster members and another member (highlighted in Figure 1), is coincident with strong mid-/far infrared emission. Assuming all of the infrared flux could be attributed to the same object, Webb et al. (2015a) measured an SED-fitted star formation rate of $860 M_{\odot} \text{ yr}^{-1}$, after correcting for AGN contamination. However, the data used to calculate the star formation rate and build the spectral energy distribution (SED) suffer from poor spatial resolution (several to tens of arcsecs), and moreover, the centroid of the $24 \mu\text{m}$ *Multiband Imaging Photometer* (MIPS) data used in this calculation is located approximately 15 kpc (1.75 arcsec) to the South-East of the BCG centre. Therefore, it is still unclear how extended, clumpy and where exactly is the star formation in the core of SpARCS1049. Hereafter, we will refer to this region of star formation as the star formation in the vicinity of the BCG.

Recently, a large reservoir of cold molecular gas ($M_{\text{H}_2} = 1.1 \pm 0.1 \times 10^{11} M_{\odot}$) was discovered in the central region of SpARCS1049 (based on a source brightness temperature of $1.16 \pm 0.10 \times 10^{11} \text{ K km s}^{-1} \text{ pc}^2$; Webb et al. 2017). The CO-to-H₂ conversion factor used is $\alpha_{\text{CO}} = 0.8 M_{\odot} (\text{K km s}^{-1} \text{ pc}^2)^{-1}$, providing a conservative estimate of the mass: α_{CO} could be as high as $4.0 M_{\odot} [\text{K km s}^{-1} \text{ pc}^2]^{-1}$ (Carilli & Walter 2013), yielding to a mass of $M_{\text{H}_2} = 5.5 \pm 0.5 \times 10^{11} M_{\odot}$. However, the beam, with a full width half-maximum of 25 arcsec, is too wide to constrain more precisely the gas location and extent. This gas could be fuelling the star formation through a galaxy merger with the BCG, but the lack of multiple velocity peaks, as might be expected in a major merger, as well as the immense amount of molecular gas, opens the door to other scenarios. For example, the core morphology and the gas reservoir could have been produced by the stripping of several smaller galaxies in the cluster centre. Another explanation is that a collision with an infalling galaxy disrupted the feedback mechanisms of the AGN in the BCG, triggering a cooling flow.

To explore the radio properties of this unique cluster and further constrain the location of the star-forming zone, we present deep, multiwavelength *Karl G. Jansky Very Large Array* (JVLA) observations of SpARCS1049. Although a wide-field image has been obtained, we focus our analysis on the BCG and its vicinity. In Section 2, we present the observations and data reduction of the JVLA datasets. In Section 3 we analyze the radio data and in Section 4 we discuss the results. Finally, we present a summary in Section 5. Throughout this paper, we assume $H_0 = 69.6 \text{ km s}^{-1} \text{ Mpc}^{-1}$, $\Omega_{\text{M}} = 0.286$ and $\Omega_{\Lambda} = 0.714$. At the redshift of the source ($z = 1.7089$, Webb et al. 2015a), 1 arcsec corresponds to 8.610 kpc.

2 OBSERVATIONS AND DATA REDUCTION

2.1 VLA observations and data reduction

In 2016, we were awarded 6.5 hours of observations on the *Karl G. Jansky Very Large Array* (project 16A-283, PI Hlavacek-Larrondo). Observations, array configurations and on-source time are presented in Table 1. Centred on the BCG in SpARCS1049, the observations consisted of 2 hours in L band (1-2 GHz), two observations of 1.5 hours each in C band (4-8 GHz) and 1.5 hours in X band (8-12 GHz). RMS noise, beam FWHMs (hereafter simply referred to as *beams*) and po-

Table 1. VLA observations.

Date	Frequency (Band) (GHz)	Bandwidth (GHz)	Configuration	On-source time (min)	Flag percentage (%)	RMS ^a $\mu\text{Jy beam}^{-1}$
2016 Nov 19	1.5 (L)	1	A	80	60	11
2016 May 20 & 21	6 (C)	4	B	54	45	3 ^b
2016 May 21	6 (C)	4	B	54	52	
2016 May 21	10 (X)	4	B	54	28	4

^a Local noise level.^b Local noise level for the merged image at 6 GHz.

sition angles for the final reduced images are provided in Table 2, in the third, fourth and fifth column respectively.

Data reduction was performed with CASA (Common Astronomy Software Application, McMullin et al. 2007) following the steps described below. Most of the data reduction was performed with CASA 4.7.2, but final image in the X band was made with version 5.1.2.

First, corrupted antennae listed in the operator logs were removed. Then, prior to the automatic RFI flagging procedure, data were pre-calibrated using the tasks GAINCAL, BANDPASS and APPLYCAL. For each antenna, we examined the amplitude versus frequency plot with PLOTCAL and flagged any abnormally low or high visibilities. We then proceeded with automatic RFI excision using the RFLAG and EXTEND modes of the task FLAGDATA. The TFCROP mode was used on the most RFI affected spectral windows and further flagging was made with the MANUAL mode. After calibration, target data were split.

Images were made with the task CLEAN, using a W-projection algorithm (mode WIDEFIELD) and 480 w-planes to correct the sky curvature across the field of view (Cornwell et al. 2008). We used Briggs weighing and a robustness parameter of 0, although we tested other parameters in Section 2.2. To ensure a sufficient sampling of the respective beams, we used a pixel size of 0.25 arcsec in L band, 0.20 arcsec in C bands and 0.15 arcsec in X band. For each band, the first clean was performed using the interactive mode, which allowed the creation of a customised cleaning mask. We then applied a self-calibration procedure to the initial image. This procedure consists of deriving phase corrections with GAINCAL, applying them to the data using APPLYCAL and then making a new image. We tested several time solution intervals and solving procedures, and varied the number of self-calibrations performed. The deepest images were obtained with one round of self-calibration and a T Jones solving procedure applied to an infinite time solution interval. The two datasets in C band were imaged, self-calibrated and then re-imaged separately. Then, they were merged using the task CLEAN, self-calibrated and merged anew. We used 100 000 iterations for merging and final cleans, except in X band where the final clean was performed with 45 000 iterations. The last column of Table 1 summarizes the local noise level reached in each image. Essentially, considering the exposure times and percentage of flagged data, we were able to reach the thermal noise in each of the images. The central region surrounding the BCG is shown in Figure 1.

2.2 Additional imaging of the VLA datasets

To further search for evidence of extended radio emission (which might be related to star formation associated with the BCG), we made additional images using different resolutions

and Briggs parameters. First, we produced images with identical pixel sizes (0.25 arcsec) and beams for all frequencies (L, C and X bands). We set the parameter RESTORINGBEAM to be identical to the default L band beam, $1.27 \times 0.85 \text{ arcsec}^2$ at an angle of -81 deg . We then compared the fluxes pixel by pixel. We found no traces of faint or diffuse emission beyond the detected point sources.

Our second test consisted of degrading the resolution of the L band image, in order to better capture faint, extended emission. We applied the same imaging procedure as in Section 2.1, except for the last clean, where the resolution was degraded to 2 arcsec per pixel. We also made two other tests in L band, this time changing the Briggs robustness parameter. In one test, the robust parameter was set to -2 , which is equivalent to a uniform weighting (i.e. provide a better resolution but less sensitivity). In the other case, the robustness parameter was set to 2, equivalent to natural weighting (better sensitivity at the expense of the resolution). None of these additional images show conclusive traces of extended emission beyond the BCG point source. This remains the case if we apply similar procedures to the C and X band images.

Finally, because we were able to reach a very low noise level in the C band merged image at 6 GHz, in addition to clearly detecting the BCG, we decided to split the two original datasets (those presented in Table 1). Each dataset, spanning 4 GHz to 8 GHz, was divided into two sub-datasets: one spanning 4 to 6 GHz and another spanning 6 to 8 GHz. We merged datasets with identical frequencies following the procedure explained in the last section: separate self-calibration and imaging, then two imaging with both datasets with a self-calibration procedure intercalated. Two images, respectively centred at 5 GHz and 7 GHz, were hence created, providing two additional flux densities to constrain the BCG spectral index. Details of the BCG detection, noise and beam dimension of these images are given in Table 2. Signal-to-noise ratios in the L and X band are both below 6σ and therefore unlikely to yield to a 3σ BCG detection if split in two. Hence, we did not proceed with such a decomposition in these bands. From now on, we will specify the frequency when referring to a C band image, to avoid any confusion.

3 RESULTS AND ANALYSIS

3.1 Source Detection and Characterization within the Vicinity of the BCG

We detected radio emission coincident with the BCG optical centre at $\gtrsim 3\sigma_{\text{RMS}}$ in each of our 5 radio images. The details of these detections are outlined in Table 2 and shown in Figure 1. Although no other radio source is detected at or above $3\sigma_{\text{RMS}}$ in more than one band within 70 kpc (8 arcsec) of the BCG (to confirm a radio source, we required de-

tections in at least two bands), we detected 2 spectroscopically confirmed clusters members as point sources. They lie East of the BCG at $10 : 49 : 26.40 + 56 : 40 : 14.98$ and $10 : 49 : 32.25 + 56 : 40 : 51.53$ (J2000).

Thus, within the BCG vicinity, the flux density of radio emission coincident with other optical sources does not exceed $3\sigma_{\text{RMS}}$ in two bands or more (see the second column of Table 3).

To understand the origin of the radio emission of the BCG, we analyzed its radio spectrum (see Figure 2). Although the point-like morphology of the detection and its coincidence with the optical centre of its *HST* counterpart suggest that we detected an AGN, we do not exclude the possibility of a compact starburst. Indeed, compact starbursts are common in star-forming galaxies at $z \sim 2$ (e.g. Elbaz et al. 2011; Barro et al. 2013; Elbaz et al. 2018). In addition, several simulations of galaxy wet mergers (e.g. Di Matteo et al. 2007; Hopkins et al. 2013) found that the bulk of the post-merging starbursts occur at the centres of the newly formed galaxies.

Given that we have only five measured flux points we limit our radio SED fit to a simple power law:

$$S_{\text{model}} = AV^{\alpha} \quad (1)$$

where S is the flux density, A a coefficient and α the spectral index. This is appropriate for core or jet emission, as well as star formation, depending on the spectral index. The best fit for the BCG (see Figure 2) has a spectral index of -0.44 , with a 1σ uncertainty of 0.29 . For the other members, we obtain spectral indexes of -0.53 ± 0.19 and -0.76 ± 0.35 respectively.

The spectrum of radio emission related to star formation tends to be steeper than our BCG best fit, with spectral indexes $-0.8 < \alpha < -0.7$ (e.g. Heesen et al. 2014), but still overlap with its 1σ confidence interval. Therefore, we cannot rule out the compact starburst hypothesis based solely on the spectral index. However, the $24 \mu\text{m}$ emission, used by Webb et al. (2015a) as a tracer of the star formation, has a centroid that lies to the south-east of the BCG (~ 15 kpc from the BCG optical centre), rather than on the BCG optical - and radio - centre. Additionally, we note that the radio flux detected from the BCG is inconsistent with the star-forming spectral energy distribution fit to the infrared emission (shown in Figure 2) at $\sim 6\sigma$. Together, these points suggest that the radio emission inside the BCG is powered by an AGN.

3.2 Star Formation Rate Limits

For each of our 5 radio images, the flux densities corresponding to 3 times the noise (derived in last section and displayed in the second column of Table 3) can be used to compute an upper limit to the star formation rate (SFR) per beam i.e. the threshold above which radio emission from star formation would have been detected (see Table 3). First, we must convert those flux densities into k -corrected 1.4 GHz luminosities using (e.g. van Weeren et al. 2014; Delhaize et al. 2017):

$$L_{1.4\text{GHz}} = \frac{4\pi D_L^2}{(1+z)^{\alpha+1}} \left(\frac{1.4}{\nu_{\text{band}}} \right)^{\alpha} S_{\text{band}} \quad (2)$$

where $L_{1.4\text{GHz}}$ is in W Hz^{-1} , D_L is the luminosity distance, α the spectral index, ν_{band} is the image frequency in GHz and S_{band} is the flux density in $\text{W Hz}^{-1} \text{m}^{-2}$. Here, we assume a spectral index of -0.7 , typical for star-forming regions (e.g. Heesen et al. 2014).

These $3\sigma_{\text{RMS}}$ upper limits of the k -corrected 1.4 GHz luminosities can now be used to compute upper limits on the star formation rate within one beam, using the relation of Condon et al. (2002):

$$\text{SFR} = 1.20 \times 10^{-21} L_{1.4\text{GHz}} \quad (3)$$

where the star formation rate (SFR) is in $\text{M}_{\odot} \text{yr}^{-1}$ and $L_{1.4\text{GHz}}$ is, as before, in W Hz^{-1} . We used a Salpeter initial mass function to compute the conversion factor. Results are presented in the third column of Table 3, which also displays the results of a similar computation, starting this time with radio flux densities equivalent to $5\sigma_{\text{RMS}}$. The C band image at 6 GHz places the lowest constraint on the star formation rate within one beam ($480 \text{M}_{\odot} \text{yr}^{-1} \text{beam}^{-1}$; Table 3, column 3), but, to confirm a radio source, we required detections in at least two bands. Hence, we will consider the SFR upper limit to be $600 \text{M}_{\odot} \text{yr}^{-1} \text{beam}^{-1}$ (L band detection threshold).

4 DISCUSSION

4.1 Comparison to other BCGs

We compare the radio emission from the BCG in SpARCS1049 with the radio luminosities of the lower redshift BCGs from the Hogan et al. (2015) line-emitting sample (mean redshift $z = 0.12$). They determined the properties of about 250 $z \lesssim 0.4$ BCGs, half of them line-emitting, to explore if and how the radio properties of BCGs in relaxed clusters differ from those of BCGs in more disturbed clusters. These authors use the presence or absence of emission lines (especially $\text{H}\alpha$ and $[\text{NII}]$) as a proxy to distinguish between clusters with strong cool cores and those with weak or no cool cores. Given the intense star formation detected in SpARCS1049 BCG (Webb et al. 2015a), these criteria would imply the presence of a cool core in this BCG (see Rhea et al., in preparation for a discussion of this source's X-ray properties).

Since the steep, non core component usually dominates the overall BCG radio emission at low frequencies, Hogan et al. (2015) use the 1 GHz emission to characterize the non-core component. Conversely, the flat, core component usually dominates the BCG radio emission at higher frequencies. Hogan et al. (2015) hence use the 10 GHz emission to characterize the core component. Figure 3 presents the core and non core luminosities of the line-emitting BCGs in Hogan et al. (2015). The colours and shapes of the symbols indicate the various models used by Hogan et al. (2015) to perform the luminosity decompositions.

We are unable to perform a detailed luminosity decomposition of the radio emission in SpARCS1049 because of the lack of spectral coverage. We therefore test two limiting cases. We first assume that all the emission we observed in the BCG comes from AGN jets and follow the spectral index computed in Section 3.1. Based on the emission level at 1.5 GHz in the observer frame, we computed the k -corrected jet emission at 1 GHz. Then based on the k -corrected jet emission at 10 GHz, we compute an upper limit for the core emission. The result is shown in gold on Figure 3. We then assume that all the observed radio emission in the BCG comes from the AGN core. Following a similar procedure, we compute a k -corrected core emission at 10 GHz and an upper limit for the jet emission at 1 GHz. The result is shown in pink on Figure 3.

Figure 3 shows that the BCG in SpARCS1049 lies in the middle of the dot cloud, no matter how the emission

Table 2. BCG detection.

Frequency (GHz)	Integrated flux (μJy)	Peak ($\mu\text{Jy beam}^{-1}$)	RMS ($\mu\text{Jy beam}^{-1}$)	Beam FWHM (arcsec \times arcsec)	PA ^a (deg)
1.5	50 ± 21	42 ± 11	11	1.27×0.85	-81
5	29.1 ± 9.8	20.6 ± 4.1	5	1.25×0.90	40
6	28.4 ± 8.7	14.8 ± 3.0	3	1.04×0.73	38
7	23.5 ± 8.7	21.8 ± 4.7	5	0.95×0.33	37
10	21.9 ± 6.5	21.5 ± 3.6	4	0.72×0.46	81

^a Position angle of the beam, measured counter-clockwise from North to East.

Table 3. Minimal star formation rate detectable for each image.

Frequency (GHz)	$3\sigma_{\text{RMS}}$ flux density upper limit ($\mu\text{Jy beam}^{-1}$)	3σ SFR upper limit ($M_{\odot} \text{ yr}^{-1} \text{ beam}^{-1}$)	5σ SFR upper limit ($M_{\odot} \text{ yr}^{-1} \text{ beam}^{-1}$)
1.5	32	600	990
5	14	590	990
6	10	480	800
7	14	780	1310
10	11	790	1320

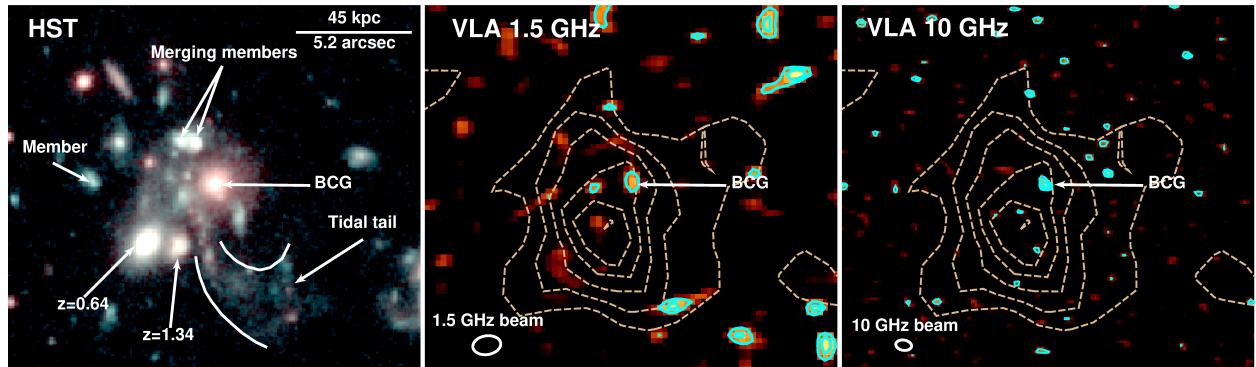


Figure 1. Deep VLA images of the BCG in SpARCS1049 and its *HST* counterpart. Left: A composite *HST* infrared image (F105W in blue and green, F160W in red; for the data reduction see Webb et al. 2015a) of the centre of SpARCS1049. We highlight 3 cluster members, 2 foreground galaxies, the tidal tail and the BCG. Middle: 1.5 GHz VLA image of the same area ($\sigma_{\text{RMS}} = 10.5 \mu\text{Jy beam}^{-1}$). Right: 10 GHz VLA image ($\sigma_{\text{RMS}} = 3.7 \mu\text{Jy beam}^{-1}$). No extended emission is detected in any image. The scale is indicated in the top right corner of the *HST* image. The VLA beams are shown in the lower left corners. The radio contours ($3, 4$ and $5\sigma_{\text{RMS}}$ levels) are displayed in cyan and the *Spitzer* MIPS $24 \mu\text{m}$ contours are overlotted in beige.

is distributed between jets and core. Therefore, the BCG in SpARCS1049 has a radio luminosity typical of BCGs at $z \leq 0.4$, which is somewhat surprising. Since SpARCS1049 hosts a $\sim 10^{11} M_{\odot}$ molecular gas reservoir (Webb et al. 2017), and radio AGN tend to be more common and more luminous at $z \sim 1.5$ (Smolčić et al. 2017), we expected the BCG of SpARCS1049 to lie among the luminous BCGs of the Hogan et al. (2015) sample.

More quantitatively, we can compare the SpARCS1049 BCG to the 1.4 GHz luminosity function. Smolčić et al. (2017) calculated that the 1.4 GHz rest-frame characteristic luminosity for AGN with luminosities between 10^{22} and $10^{24} \text{ W Hz}^{-1}$ is $L^*(z) \propto (z+1)^{(2.88 \pm 0.82) - (0.84 \pm 0.34)z}$ with $L^* = 10^{24.59} \text{ W Hz}^{-1}$ locally. This yields to $L^* = (1.64 \pm 0.51) \times 10^{25} \text{ W Hz}^{-1}$ at the cluster redshift. Assuming the simple power law model computed in Section 3.1, the BCG has a rest frame 1.4 GHz luminosity of $6.4 \pm 3.0 \times 10^{23} \text{ W Hz}^{-1}$, more than an order of magnitude below the characteristic luminosity of Smolčić et al. (2017).

Therefore, the black hole at the centre of the BCG must

have a modest accretion rate. This relatively low luminosity suggests that something may prevent or partially block inflows from the molecular gas reservoir. Among the possible culprits: an efficient star formation or an offset between the gas reservoir and the BCG.

4.2 Star formation in the vicinity of the BCG

After a tentative characterization of the detected AGN, the obvious question is: where is the intense star formation indicated by the infrared emission? Webb et al. (2015a) computed an AGN-corrected star-forming rate of $860 \pm 130 M_{\odot} \text{ yr}^{-1}$, based on the far infrared emission (FIR), computed from the SED fitting. A comparison between our VLA and the Webb et al. (2015a) spectral energy distributions is displayed in Figure 2 and summarized in Table 4. This Figure reveals that the measured radio fluxes are significantly below Webb et al. (2015a) SED fit. A computation of the reduced χ^2 (χ^2_{ν}) of the radio data with respect to the best-fitting SED gives $\chi^2_{\nu} = 9.5$, which correspond to an offset of 6σ . Also, the ex-

Table 4. Summary of the best-fitting SEDs.

Fit	χ^2_{ν}	60 μm flux (mJy)	Uncorrected SFR ($M_{\odot} \text{ yr}^{-1}$)	SFR ^a ($M_{\odot} \text{ yr}^{-1}$)
IR & radio	1.86	13 ± 1	467 ± 29	374 ± 23
IR only	0.44	40^{+9}_{-6}	1074 ± 162	859 ± 130

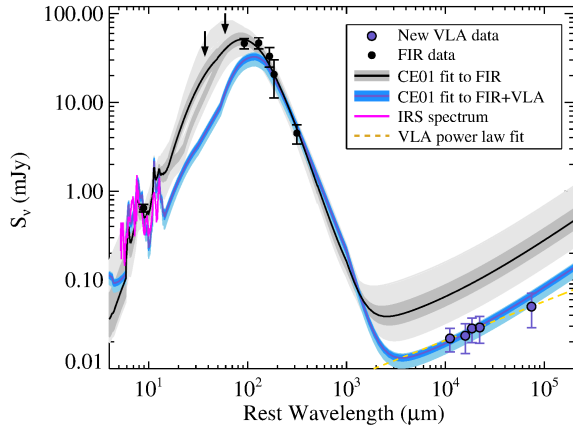
^a Assuming a 20% AGN contribution.

Figure 2. A comparison between Webb et al. (2015a) best-fitting SED (in black) and the best infrared and radio fit (in blue). Both fits are based on Chary & Elbaz (2001) templates. The shaded region encloses all the SED variations within 68% (medium grey and blue) and 95% (lighter grey and blue) surface contour of the normalized χ^2 probability distribution. The magenta line is the Infrared Spectrograph (IRS) spectrum from Webb et al. (2015a). In addition to the *Spitzer* MIPS 24 μm data, the far-infrared data and limits are from the Photoconductor Array Camera and Spectrometer (PACS) and the Spectral and Photometric Imaging Receiver (SPIRE) onboard *Herschel Space Observatory* and from the Submillimetre Common-User Bolometer Array 2 (SCUBA-2) on James Clerk Maxwell Telescope. The dashed yellow line shows the power law best fit to the radio point. There is an offset of approximately 6σ between the VLA data and the original infrared-only fit.

pected spectral indexes, both around -0.7 , are slightly steeper than the observed index, -0.44 ± 0.29 .

To investigate whether or not a different SED template could better fit the radio data, we performed our own fit of far-infrared and radio data, following Webb et al. (2015a) method (also described in Noble et al. 2016): we tested each Chary & Elbaz (2001) templates over a range of amplitudes, generating a 2D-grid of fits. We select the best fit based on its χ^2 probability. In Figure 2, the dark shaded regions correspond to all fits enclosed within the 68% surface contour of the normalized χ^2 probability distribution and the lighter shades correspond to all fits within 95%. The reduced χ^2_{ν} of the best fit is 1.86, corresponding to an integrated χ^2 probability value of 0.05. Hence, we can reject the possibility that the fit accurately described the data with 95% confidence. By contrast, with a χ^2_{ν} of 0.44, the infrared-only fit can be rejected with 20% confidence only. It is worth noticing that the infrared and radio fit provides a better estimation of the radio flux, although slightly too steep to match with the best-fitting power law. However, it significantly underestimates the far infrared emission: the 60 μm flux derived from the infrared-only fit is 3 times greater than the flux estimated from the radio and

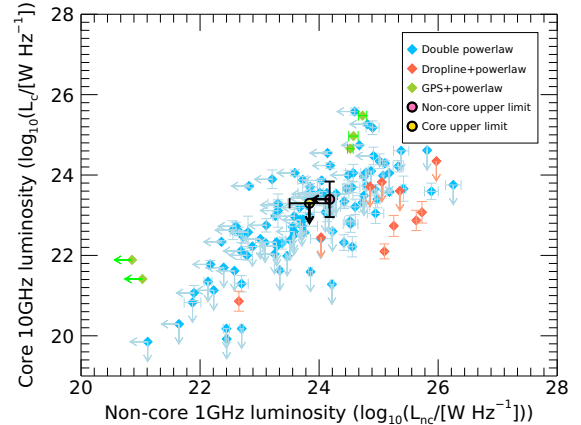


Figure 3. A comparison between core and a non-core powers of the Hogan et al. (2015) sample and 2 possibilities for SpARCS1049. Blue diamonds are Hogan et al. (2015) objects following a power law model for non-core and core emission and coral diamonds non-core emission follow a ‘dropline model’, associated with a power law model for core emission. Green diamond models for non-core emission are power laws, but their core emission follow gigahertz peaked source (GPS) models. Assuming that most of the emission from SpARCS1049 BCG originates from one component, we derived an upper limit for the non-core component (pink circle) and the core component (gold circle).

infrared fit (see Table 4). Therefore, no template seems to be consistent with both far infrared and radio emission.

This mismatch suggests that far infrared emission is tracing a different phenomenon than the radio. Since the radio emission probably comes from the AGN (see Section 3.1), the far infrared emission might be dominated by star formation. Moreover, most of the mid and far-infrared measurements have resolutions spawning from several to tens of arcsecs, while our biggest radio beam spans $1.27 \text{ arcsec} \times 0.85 \text{ arcsec}$. Keeping this in mind, we suggest that the star formation happens close to the BCG but not within it. If the star formation had been within the BCG, we would have detected it (the BCG is a point source) and the new SED fit would have been more consistent with the far infrared data.

To explore the extent or possible ‘clumpiness’ of this star-forming zone, we used the Yun et al. (2001) relation between far infrared (60 μm) and 1.4 GHz luminosity. Figure 4 shows the Yun et al. (2001) data and relationship, with 3 overplotted upper limits corresponding to 1, 4 and 10 star-forming ‘clumps’. We assume that each ‘clump’ contributes equally to the FIR emission, while in radio they could be resolved. We set the radio flux upper limit to $5.0 \times 10^{23} \text{ W Hz}^{-1}$ ($600 M_{\odot} \text{ yr}^{-1}$), in agreement with the L band detection threshold (see Section 3.2).

The star-forming region is likely to be clumpy, since the

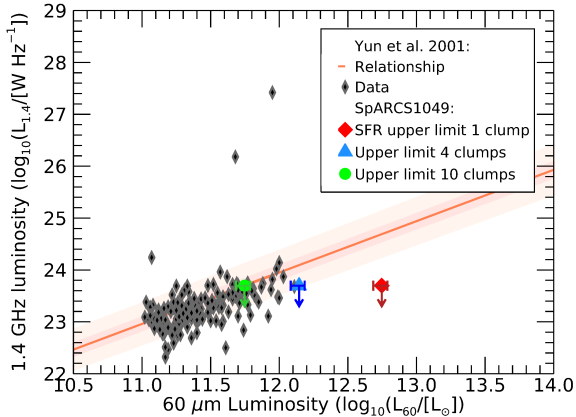


Figure 4. Comparison between Yun et al. (2001) (the 1 and 3σ uncertainties are displayed as coloured regions) and our upper limit for star formation detection, as calculated in Section 3.2. The upper limits in red blue and green show what happens when we vary the number of star formation ‘clumps’, based on the assumption that these clumps could be resolved in radio (so the detection limit does not change in radio), but are all within one beam in the infrared. We also assume that all ‘clumps’ contribute equally to the $60\ \mu\text{m}$ emission. The $60\ \mu\text{m}$ luminosity calculation is based on the best-fitting infrared SED. To be consistent with our SED-based star-forming rates, the AGN far-infrared luminosity is subtracted from the FIR luminosities presented here, assuming a 20 per cent contribution (Webb et al. 2015a).

10 clumps upper limit lies on the relationship while the 4 clumps upper limit is on the edge of its 3σ region. This is consistent with a non-detection: with a star formation rate of $860 \pm 130\ \text{M}_{\odot}\ \text{yr}^{-1}$, the star-forming zone is not detectable as long as it spreads over two VLA radio beams or more. This would be consistent with the star formation being distributed across the ‘beads on a string’ optical feature. We don’t expect the star formation to be spread across the cluster galaxies in the beam: excluding the BCG, there is only 3 cluster members within the MIPs beam, none of them situated at less than ~ 30 kpc (~ 3.5 arcsec) of the detection centroid (see Figure 1).

4.3 Implications for BCG formation scenarios

Although the *HST* mosaic revealed a morphology consistent with a merger-induced starburst (Webb et al. 2015a), this scenario is disfavoured by our constraints on star formation. Di Matteo et al. (2007) and Hopkins et al. (2013) found that most of the post-merger starburst occurs in the centre of the newly formed galaxy. In SpARCS1049, the bulk of the star formation is likely occurring outside of the BCG. Moreover, the AGN in the BCG is not very active, which is weak evidence against this scenario: major galaxy interactions can trigger radio-mode AGN (Ellison et al. 2015). However, they are not the main causes of AGN activity, as only $16.7_{-3.5}^{+5.3}\%$ of the radio-AGN hosts are highly disturbed, a fraction consistent with the amount of non-active interacting galaxies (Kocevski et al. 2012). Besides, the gas reservoir in SpARCS1049 seems too large to originate from gas-rich mergers (e.g. Edge 2001; McDonald et al. 2013) and lacks the multiple velocity components induced by such events (Webb et al. 2017).

To explain the presence of a $1.1 \pm 0.1 \times 10^{11}\ \text{M}_{\odot}$ gas reservoir in the centre of SpARCS1049, Webb et al. (2017)

suggested two other scenarios: 1) several smaller galaxies stripped of their gas by the BCG or 2) a cooling flow. While the first scenario cannot be rejected or confirmed by our radio data, the second scenario raise the possibility of a high-redshift Phoenix cluster analogue.

The Phoenix cluster hosts the only other well-studied high redshift BCG with a comparable star formation rate. At $z=0.596$, its BCG hosts a massive cooling flow of $3820 \pm 530\ \text{M}_{\odot}\ \text{yr}^{-1}$ fuelled by a molecular gas reservoir (dihydrogen) of $2.1 \pm 0.3 \times 10^{10}\ \text{M}_{\odot}$ and forms stars at a rate of $610 \pm 50\ \text{M}_{\odot}\ \text{yr}^{-1}$ (see McDonald et al. 2012, 2013, 2014, 2015; Ueda et al. 2013; Tozzi et al. 2015; Russell et al. 2017). By comparison, SpARCS1049 has a SFR of $860 \pm 130\ \text{M}_{\odot}\ \text{yr}^{-1}$ and a ~ 5 times more massive molecular gas reservoir.

Despite such a large gas reservoir to fuel AGN feedback, the total 10 MHz to 10 GHz integrated power of SpARCS1049 central AGN is about $4.4 \pm 3.5 \times 10^{33}\ \text{W}$. In contrast, the radio power emitted by the jets in the Phoenix cluster is ~ 1000 times stronger ($3.6 \times 10^{36}\ \text{W}$; McDonald et al. 2015). This suggests that, if there is a substantial cooling flow in the centre of SpARCS1049, only a small fraction of the inflowing gas reaches the centre of the BCG in SpARCS1049. Thus, if SpARCS1049 has a cooling flow, there might be a significant offset between the BCG and the gravitational centre of the cluster. Hamer et al. (2012) and Vantyghem et al. (2019) suggested that the sloshing motion due to a galaxy interaction can trigger gas condensation offsetted from the BCG. A similar history could explain the presence of molecular gas in the core of SpARCS1049, although Vantyghem et al. (2019) argue that the condensation of all the intracluster medium within 10 kpc of the centre of the cluster is required to create a $10^{10}\ \text{M}_{\odot}$ gas reservoir in RXJ0821+0752. Therefore, additional mechanisms might be needed to explain the gathering of $10^{11}\ \text{M}_{\odot}$ of cold gas in SpARCS1049. Alternatively, the AGN weakness may originate from a very efficient star formation in SpARCS1049.

5 SUMMARY

We presented deep, multiwavelength JVLA radio observations of SpARCS1049, one of the most distant galaxy clusters ever studied in radio. SpARCS1049 is a cluster of galaxies with a starbursting core, displaying a complex morphology in the infrared (Webb et al. 2015a) and a immense $\sim 10^{11}\ \text{M}_{\odot}$ molecular gas reservoir (Webb et al. 2017). We detected the BCG at 1.5, 5, 6, 7 and 10 GHz, but we did not detect any diffuse emission or starbursting clump outside of the core. Given that, we draw the following conclusions:

The radio emission of the BCG likely comes from its AGN. It is best fit by a simple power law, with a spectral index of -0.44 ± 0.29 and has a radio luminosity consistent with the average luminosity of the lower redshift BCG sample of Hogan et al. (2015).

We found an offset of 6σ between our new VLA data and the SED fit previously made (Webb et al. 2015a). Moreover, our best infrared & radio fit underestimates the far infrared fluxes and can be rejected with 95% confidence based on the integrated χ^2 probability. This suggests that star-forming regions are not embedded in the BCG. Combining the SED fit with our upper limit for the radio emission induced by star formation, we find that star-forming regions are either made of numerous clumps or very extended.

We explore the possible origins of the BCG complex infrared morphology and of its gas reservoir. There is growing

evidence against the single, major wet merger scenario initially developed by Webb et al. (2015a). Although a cooling flow fits well with our constraints on the star-forming regions, X-ray data are needed to distinguish between this scenario and the gas stripping of multiples galaxies.

ACKNOWLEDGEMENTS

We acknowledge support from the NRAO helpdesk for data reduction bugs and from Tracy Clarke for persistent data reduction bugs. We wish to thank also Michael McDonald for sharing information about the Phoenix Cluster and Mark Voit for being the first to invoke the possibility of a cooling flow. AT is supported by the NSERC Postgraduate Scholarship-Doctoral Program. TMAW and JHL acknowledge the support of an NSERC Discovery Grant and of the FRQNT. JHL is also supported by NSERC through the Canada Research Chair programs. MM acknowledges support from the Spanish Juan de la Cierva program (IJCI-2015-23944). GW is supported by the National Science Foundation through grant AST-1517863, by *HST* program number GO-15294, and by grant number 80NSSC17K0019 issued through the NASA Astrophysics Data Analysis Program (ADAP). Support for program numbers GO-13677/14327.01 and GO-15294 was provided by NASA through a grant from the Space Telescope Science Institute, which is operated by the Association of Universities for Research in Astronomy Incorporated, under NASA contract NAS5-26555.

References

Barro G., et al., 2013, *ApJ*, 765, 104
 Bellstedt S., et al., 2016, *MNRAS*, 460, 2862
 Bildfell C., Hoekstra H., Babul A., Mahdavi A., 2008, *MNRAS*, 389, 1637
 Carilli C. L., Walter F., 2013, *ARA&A*, 51, 105
 Chary R., Elbaz D., 2001, *ApJ*, 556, 562
 Condon J. J., Cotton W. D., Broderick J. J., 2002, *AJ*, 124, 675
 Cornwell T. J., Golap K., Bhatnagar S., 2008, *ISTSP*, 2, 647
 Croton D. J., et al., 2006, *MNRAS*, 365, 11
 De Lucia G., Blaizot J., 2007, *MNRAS*, 375, 2
 Delhaize J., et al., 2017, *A&A*, 602, A4
 Demarco R., et al., 2010, *ApJ*, 711, 1185
 Di Matteo P., Combes F., Melchior A.-L., Semelin B., 2007, *A&A*, 468, 61
 Donahue M., et al., 2007, *ApJ*, 670, 231
 Dressler A., 1978, *ApJ*, 223, 765
 Edge A. C., 2001, *MNRAS*, 328, 762
 Elbaz D., et al., 2011, *A&A*, 533, A119
 Elbaz D., et al., 2018, *A&A*, 616, A110
 Ellison S. L., Patton D. R., Hickox R. C., 2015, *MNRAS*, 451, L35
 Elmegreen D. M., Elmegreen B. G., Ferguson T., Mullan B., 2007, *ApJ*, 663, 734
 Fabian A. C., 1994, *ARA&A*, 32, 277
 Fabian A. C., Walker S. A., Russell H. R., Pinto C., Sanders J. S., Reynolds C. S., 2017, *MNRAS*, 464, L1
 Hamer S. L., Edge A. C., Swinbank A. M., Wilman R. J., Russell H. R., Fabian A. C., Sanders J. S., Salomé P., 2012, *MNRAS*, 421, 3409
 Heesen V., Brinks E., Leroy A. K., Heald G., Braun R., Bigiel F., Beck R., 2014, *AJ*, 147, 103
 Hlavacek-Larrondo J., Fabian A. C., Edge A. C., Ebeling H., Sanders J. S., Hogan M. T., Taylor G. B., 2012, *MNRAS*, 421, 1360
 Hogan M. T., et al., 2015, *MNRAS*, 453, 1201
 Hopkins P. F., Cox T. J., Hernquist L., Narayanan D., Hayward C. C., Murray N., 2013, *MNRAS*, 430, 1901

Hudson D. S., Mittal R., Reiprich T. H., Nulsen P. E. J., Andernach H., Sarazin C. L., 2010, *A&A*, 513, A37
 Kocevski D. D., et al., 2012, *ApJ*, 744, 148
 Lidman C., et al., 2012, *MNRAS*, 427, 550
 Markevitch M., Vikhlinin A., 2007, *Phys. Rep.*, 443, 1
 McDonald M., et al., 2012, *Nature*, 488, 349
 McDonald M., Benson B., Veilleux S., Bautz M. W., Reichardt C. L., 2013, *ApJ*, 765, L37
 McDonald M., et al., 2014, *ApJ*, 784, 18
 McDonald M., et al., 2015, *ApJ*, 811, 111
 McDonald M., et al., 2016, *ApJ*, 817, 86
 McMullin J. P., Waters B., Schiebel D., Young W., Golap K., 2007, in Shaw R. A., Hill F., Bell D. J., eds, *ASP Conf. Ser. Vol. 376, Astronomical Data Analysis Software and Systems XVI*. p. 127
 McNamara B. R., Nulsen P. E. J., 2007, *ARA&A*, 45, 117
 McNamara B. R., Nulsen P. E. J., 2012, *NJPh*, 14, 055023
 Muzzin A., et al., 2009, *ApJ*, 698, 1934
 Noble A. G., Webb T. M. A., Yee H. K. C., Muzzin A., Wilson G., van der Burg R. F. J., Balogh M. L., Shupe D. L., 2016, *ApJ*, 816, 48
 O’Dea C. P., et al., 2008, *ApJ*, 681, 1035
 O’Dea K. P., et al., 2010, *ApJ*, 719, 1619
 Oemler Jr. A., 1976, *ApJ*, 209, 693
 Rafferty D. A., McNamara B. R., Nulsen P. E. J., Wise M. W., 2006, *ApJ*, 652, 216
 Ragone-Figueroa C., Granato G. L., Ferraro M. E., Murante G., Biffi V., Borgani S., Planelles S., Rasia E., 2018, *MNRAS*, 479, 1125
 Rawle T. D., et al., 2012, *ApJ*, 747, 29
 Russell H. R., et al., 2017, *ApJ*, 836, 130
 Santos J. S., Tozzi P., Rosati P., Böhringer H., 2010, *A&A*, 521, A64
 Smolčić V., et al., 2017, *A&A*, 602, A6
 Stott J. P., Edge A. C., Smith G. P., Swinbank A. M., Ebeling H., 2008, *MNRAS*, 384, 1502
 Stott J. P., Collins C. A., Burke C., Hamilton-Morris V., Smith G. P., 2011, *MNRAS*, 414, 445
 Tozzi P., et al., 2015, *A&A*, 580, A6
 Tremaine S. D., Richstone D. O., 1977, *ApJ*, 212, 311
 Ueda S., Hayashida K., Anabuki N., Nakajima H., Koyama K., Tsunemi H., 2013, *ApJ*, 778, 33
 Vantyghe A. N., et al., 2019, *The Astrophysical Journal*, 870, 57
 Voigt L. M., Fabian A. C., 2004, *MNRAS*, 347, 1130
 Webb T., et al., 2015a, *ApJ*, 809, 173
 Webb T. M. A., et al., 2015b, *ApJ*, 814, 96
 Webb T., Lowenthal J., Yun M., Noble A. G., Muzzin A., Wilson G., Yee H. K. C., Cybulski R., 2017, *ApJ*, 844, L17
 Wilson G., et al., 2009, *ApJ*, 698, 1943
 Yun M. S., Reddy N. A., Condon J. J., 2001, *ApJ*, 554, 803
 Zhuravleva I., et al., 2014, *Nature*, 515, 85
 van Weeren R. J., et al., 2014, *ApJ*, 786, L17

This paper has been typeset from a $\text{\TeX}/\text{\LaTeX}$ file prepared by the author.